

Article

Tetragonal gyroid structure from symmetry manipulation: A brand-new member of the gyroid surface family



A new gyroid family member, the tetragonal gyroid surface (shifted tG), was designed on the basis of a binary self-assembly system containing diblock copolymer PS-*b*-PAA as the main building block and the small surfactant cetyltrimonium bromide (CTAB) as the structure manipulator. Featuring shifted double-gyroidal networks, shifted tG belongs to a tetragonal symmetry with the low-symmetry space group $I4_1/a$ and shows a widened photonic band gap along with shifting degrees, initiating a new gyroid symmetric system.

Shuqi Wang, Hao Chen, Tianyu Zhong, ..., Yuanyuan Cao, Yongsheng Li, Lu Han

yuanyuancao@ecust.edu.cn (Y.C.)
ysli@ecust.edu.cn (Y.L.)
luhan@tongji.edu.cn (L.H.)

Highlights

Symmetry manipulation of gyroid surfaces is realized through binary assembly system

The shifted double-gyroidal networks possess a brand-new tetragonal structure

The structure features periodic wall thickness due to local concave free energy

The tetragonal gyroid exhibits intriguing optical properties due to symmetry breaking

Article

Tetragonal gyroid structure from symmetry manipulation: A brand-new member of the gyroid surface family

Shuqi Wang,^{1,5} Hao Chen,^{2,5} Tianyu Zhong,¹ Quanzheng Deng,³ Shaobo Yang,¹ Yuanyuan Cao,^{1,*} Yongsheng Li,^{1,4,*} and Lu Han^{3,6,*}

SUMMARY

Gyroid (G) surfaces, the most famous naturally occurring triply periodic hyperbolic surfaces, are well known for their amazing properties closely associated with their intriguing symmetries. Although mathematicians and physicists are devoted to exploring new G surface family members, it remains a mystery whether any novel symmetrical G substructure can be experimentally validated beyond its well-known cubic-symmetrical systems. Herein, we report a tetragonal G substructure (shifted tG) obtained from a cooperative binary self-assembly system consisting of polystyrene-*b*-poly(acrylic acid) and cetyltrimethylammonium bromide. Shifted tG features periodic distributions of uneven matrix thicknesses with local concave free energies, exhibits an extraordinarily shifted double-gyroidal network with a low-symmetry space group of $I4_1/a$ (no. 88), and possesses shifting-degree-dependent photonic band gaps that are never present in its unshifted cubic-symmetrical counterparts. The emergence of new G structures demonstrates a new frontier in the minimal surface subject, crucial for its exploration and innovation.

INTRODUCTION

Gyroid (G) surfaces, first discovered by Alan Schoen in 1970,¹ are the most complex and functionally valuable three-dimensional (3D) geometries yet discovered in that they possess infinite, non-self-intersecting triply periodic minimal surfaces (TPMSs), or constant mean curvature surface structures.^{2–4} Since the discovery of G, the beauty of its peculiar symmetrical and geometrical features has ensured that G structured materials sparkle in interdisciplinary areas, such as mechanical (e.g., exceptionally high strength networks),⁵ catalytic (e.g., electrocatalysts and photocatalysis),^{6,7} electronic (e.g., superconductive materials and hybrid solar cell),^{8–10} and optical (e.g., antireflection, 3D photonic crystals, and chiral metamaterials)^{11–15} materials. Therefore, theoretical and experimental investigations of Gs are a long-lasting topic in interdisciplinary science. The naturally occurring G surfaces have been discovered in numerous biological systems^{4,12,16} and are regarded as paragon inspirations to learn from nature's complex design principles particularly in cell membranes and Lepidoptera wing scales.^{17–19} Attempts to artificially fabricate G surface structures include top-down approaches, such as angled etching, 3D printing, interference lithography, and two-photon polymerization,^{20–22} yet these methods are challenging in controlling submicron details. Another approach is bottom-up synthesis, such as thermotropic^{23–25} and lyotropic liquid crystals,^{26–28} block copolymer assemblies,^{13,14,29–32} and their inorganic replicas,^{33–35} whose length scales can

THE BIGGER PICTURE

Triply periodic minimal surfaces (TPMSs), the unique three-dimensional geometry characterized by infinite and non-self-intersecting periodic networks with complex symmetries, are diamonds shining in mathematics, physics, and soft matter science. Gyroid surfaces, the most appealing and complicated TPMSs, possess extraordinary properties highly associated with their symmetrical features and have inspired various terrific man-made artifacts. Manipulating the symmetry of gyroid surfaces is crucial to exploring the beauty of their geometry, but all of their known stable structures are restricted to cubic space groups. In this study, by manipulating symmetry in a designed binary self-assembly system to break the principles of thermodynamic restriction of the polymer phase separation, we obtained a brand-new tetragonal gyroid with intriguing optical properties, which opens up new avenues for generating novel materials with exceptional structures and understanding the minimal surface families.

range from a few to hundreds of nanometers, although their formation mechanisms remain obscure.

Naturally restricted by the generic symmetry-based properties, the currently known stable G surfaces (double G, single G, and alternating G) all belong to the cubic crystal system. The most frequently occurring gyroidal structure is double G, which preserves the highest symmetry with the space group cubic $Ia\bar{3}d$ (no. 230) because of its continuous surfaces with nonpositive Gaussian curvature that separates space equally into two interpenetrating labyrinths with three-coordinate nodes.^{2–4} It appears in various self-assembly systems, including the bicontinuous liquid crystal phases^{27,28} and microphase separation of most pure AB diblock, ABA, and ABC triblock copolymers.^{30–32,36,37} Extracting one of the labyrinths of double G produces a single G surface, which belongs to the lower-symmetry space group cubic $I4_132$ (No. 214), represented by the famous single-G chiral photonic crystal discovered in butterfly wing scales.^{18,19} In chemical synthesis, the single-G surface has been experimentally realized by an alternating version (alternating G) of a distinguishable dual network filled with different substances.^{38,39}

The high symmetry of G surfaces offers advantages in many aspects; in particular, the highest symmetrical double-G surfaces exhibit the most equivalent spatial organizations with such isotropic properties as more uniform mass transport and uniform mechanical responses.⁴⁰ However, exceptional material properties are often highly associated with crystal symmetries.⁴¹ For example, the symmetry breaking and phase transition in atomic double-gyroidal crystalline leucite crystals have brought this mineral a behavior close to pure ferroelasticity.⁴² In terms of optical materials, only through breaking the symmetry of double G can a series of novel materials be generated,⁴³ such as complete-band-gap photonic crystals, metamaterials, or photonic crystals exhibiting amazing Weyl points and line nodes.^{13–15,44–46}

Therefore, the fundamental understanding of the structural features of the G surface and the exploration of the new noncubic forms by symmetry breaking are crucial for this research field.^{47–50} Only recently has a tetragonal deformation of the G surface with space group $I4_1/acd$ received rigorous proof.⁵¹ However, to the best of our knowledge, the tetragonal G surface has never been experimentally identified in the biological structures or self-assembly of amphiphilic molecules. On the other hand, changing the relative positions of the two skeletons of the double G would be an effective method of altering its symmetry and achieving modulated properties. Nevertheless, Hsueh et al. achieved the symmetry breaking on the G surface only by moving the two independent gyroidal networks through artificial removal of the intervening TPMS matrix,⁵² after which random shifts of the interlocking networks proceeded in an uncontrollable manner. To date, the new organizational forms and symmetry breaking of G surface structures with specific properties are still considered to be great challenges in self-assembly fields.

Herein, we report a polymorphism for a G surface structure with a distinctive tetragonal symmetry composed of shifted networks (termed shifted tG). This structure was synthesized via aqueous copolymer self-assembly with binary components, i.e., with the linear anionic block copolymer polystyrene-*b*-poly(acrylic acid) (PS₉₂-*b*-PAA₁₆) (**Figures S1–S4** and **Tables S1–S3**) as the main building block and the small-molecular cationic surfactant cetyltrimethylammonium bromide (C₁₆TAB) as the auxiliary modulator, followed by a silicification process to generate silica replicates. Insertion of C₁₆TAB as a modulator greatly influenced the phase separation of the diblock copolymer through a competition between the original organization of immiscible

¹Laboratory of Low-Dimensional Materials Chemistry, Key Laboratory for Ultrafine Materials of Ministry of Education, Frontiers Science Center for Materiobiology and Dynamic Chemistry, Shanghai Engineering Research Center of Hierarchical Nanomaterials, School of Materials Science and Engineering, East China University of Science and Technology, Shanghai 200237, China

²Institute of Mathematical Sciences, ShanghaiTech University, 393 Middle Huaxia Road, Shanghai 201210, China

³School of Chemical Science and Engineering, Tongji University, Shanghai 200092, China

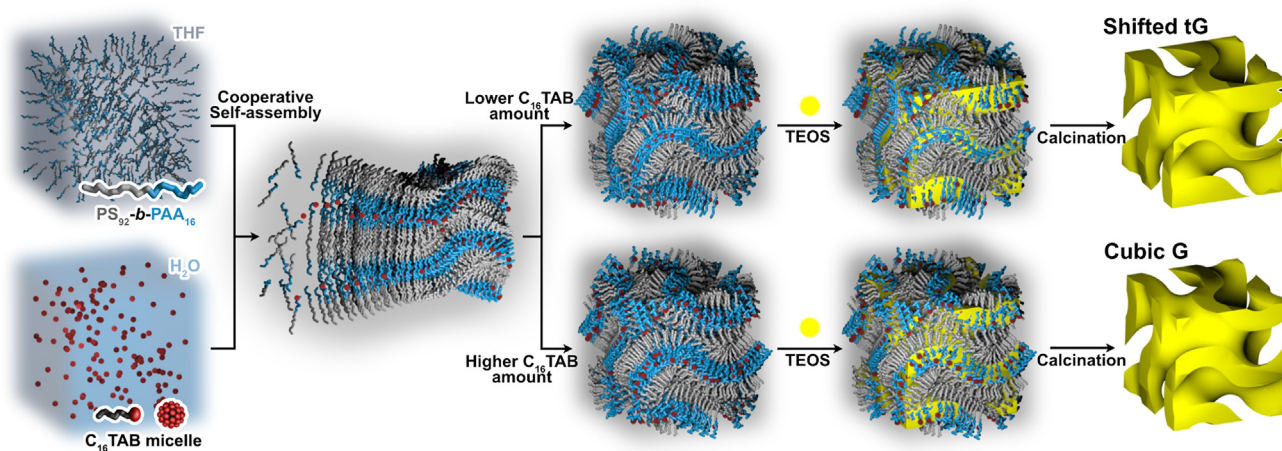
⁴School of Chemistry and Chemical Engineering, Pharmacy School, State Key Laboratory Incubation Base for Green Processing of Chemical Engineering, Shihezi University, Shihezi 832003, China

⁵These authors contributed equally

⁶Lead contact

*Correspondence:
yuanyuancao@ecust.edu.cn (Y.C.),
ysl@ecust.edu.cn (Y.L.),
luhan@tongji.edu.cn (L.H.)

<https://doi.org/10.1016/j.chempr.2023.12.017>



Scheme 1. Schematic drawing of the synthetic strategy

The shifted tG and cubic G structures can be obtained in the binary system of C₁₆TBA/PS₉₂-*b*-PAA₁₆ with different molar ratios.

blocks and additional electrostatic interactions, which led to the generation of a series of mesostructures that could not be obtained with pure diblock copolymeric assemblies. The low-symmetry tetragonal G surface appeared in a small phase region between a loose lamellar-like phase at a low C₁₆TAB/PS₉₂-*b*-PAA₁₆ ratio and a standard cubic double-G structure (termed cubic G) phase at a high C₁₆TAB/PS₉₂-*b*-PAA₁₆ ratio, and it was analyzed and assessed via detailed electron crystallography comparisons. Then, the evolution of photonic properties caused by the cubic-to-tetragonal symmetrical transition was described.

RESULTS AND DISCUSSION

Structural analysis

Aqueous phase separation of pure amphiphilic diblock copolymers has been extensively studied theoretically and experimentally.⁵³ Driven by the incompatibilities of different immiscible blocks, a cubic bicontinuous phase can be synthesized between the cylindrical and lamellar phases depending on the volume fraction of each block. In contrast to that in the pure diblock copolymer systems, phase separation in the binary system can be influenced by much more complicated parameters, which opens up versatile possibilities to generate unique morphologies and structures.^{54,55} Here, for PS₉₂-*b*-PAA₁₆ and C₁₆TAB, both hydrophobic/hydrophilic and electrostatic interactions play critical roles influencing the phase-separation behavior of PS-*b*-PAA. As shown in Scheme 1, composite micelles were initially formed through electrostatic condensation between anionic PS-*b*-PAA⁻ segments and C₁₆TA⁺ ions during the co-micellization process and then silicified to form ordered inorganic-organic hybrid aggregates. During this process, C₁₆TA⁺ ions served as the charge neutralizer/condensation agent to accelerate the aggregation of the PS₉₂-*b*-PAA₁₆ and as a bridge to connect the micelles and the silica source. We then fabricated a series of mesostructures by changing the C₁₆TAB/PS₉₂-*b*-PAA₁₆ molar ratios and removed the organic templates by calcination (Figures S5–S7). A disordered, loose lamellar-like structure was formed with a small C₁₆TAB/PAA ratio of 14.8 (mass ratio of 0.5), and lamellar/cubic intergrown structures were realized with a C₁₆TAB/PS₉₂-*b*-PAA₁₆ ratio of 29.7 (mass ratio of 1.0). A conventional cubic G was generated when the C₁₆TAB/PS₉₂-*b*-PAA₁₆ molar ratio was raised above 148.3 (mass ratio of 5.0) and finally converted to inhomogeneous disordered structures at much higher C₁₆TAB/PS₉₂-*b*-PAA₁₆ molar ratios over 237.2 (mass ratio of

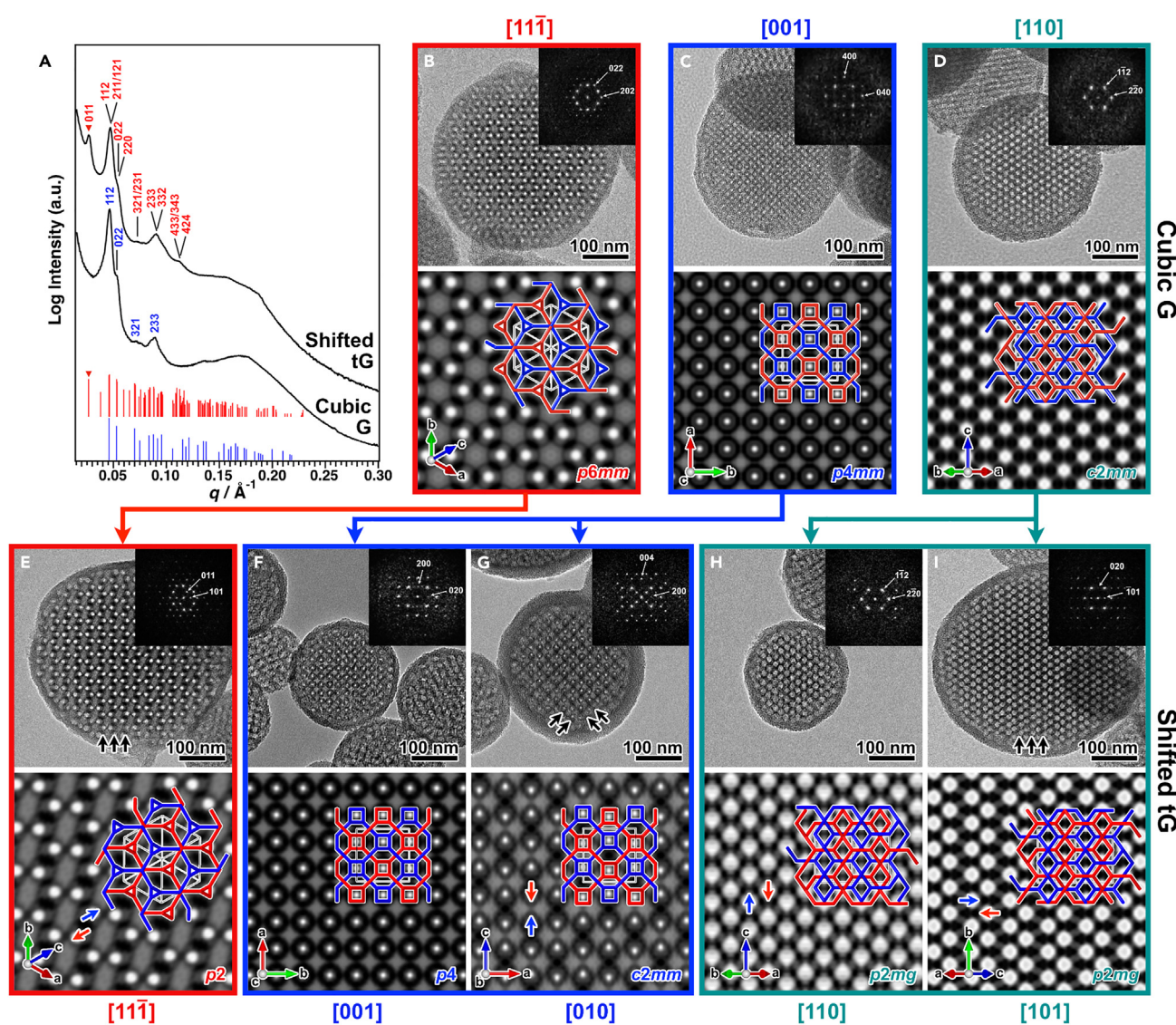


Figure 1. SAXS patterns and TEM analysis of the cubic G and shifted tG structures

(A) SAXS pattern of the cubic G and shifted tG structures. The red and blue tick markers indicate the Bragg positions obtained from the FDs. (B–D) TEM images taken from the [11̄1] (B), [001] (C), and [110] (D) directions with the corresponding FDs of the cubic G structure. (E–I) TEM images and the corresponding FDs of the shifted tG structure. As a result of symmetry breaking, the three main zone axes are mapped to five representative directions, namely the [11̄1] (E), [010] (F), [001] (G), [110] (H), and [101] (I) directions, as indicated by the red, blue, and green lines with arrows. Symmetry averaged images overlaid with the skeleton graphs are shown at the bottom of each image. The blue and red arrows show the direction of pore-channel displacement for shifted tG compared with cubic G.

8.0). In the intermediate $\text{C}_{16}\text{TAB}/\text{PS}_{92}-b-\text{PAA}_{16}$ molar ratio range of 59.3–118.6 (mass ratios of 2.0 to 4.0), the new shifted tG phase appeared.

The structure of the shifted tG phase was analyzed through a series of detailed comparisons with cubic G. In the small angle X-ray scattering (SAXS) profile (Figure 1A), cubic G synthesized with a $\text{C}_{16}\text{TAB}/\text{PS}_{92}-b-\text{PAA}_{16}$ molar ratio of 148.3 (mass ratio of 5.0) exhibited a number of reflections within the q value range of $0.04\text{--}0.25 \text{\AA}^{-1}$. The first intense peak was centered at 0.046\AA^{-1} , and the shoulder peak was at 0.053\AA^{-1} with a q ratio of $\sqrt{3}:\sqrt{4}$; they were indexed to the 112 and 022 reflections of a typical well-known double G with cubic symmetry belonging to the space group $Ia\bar{3}d$.

(no. 230), and the unit cell parameter was calculated as $a = 33.6$ nm. Interestingly, shifted tG synthesized with a C₁₆TAB/PS₉₂-*b*-PAA₁₆ molar ratio of 118.6 (mass ratio of 4.0) showed a very similar SAXS profile in the same q value range. A series of strong reflections were basically consistent with cubic G; however, an additional intense reflection centered at 0.026 Å⁻¹ revealed notable symmetry differences between the two samples. Combined with transmission electron microscopy (TEM) investigations (*vide post*), the unexpected structure of shifted tG was identified as a body-centered tetragonal crystal with the space group *I*4₁/*a* (No. 88), a subgroup of *I*4̄3*d* but with much lower symmetry. The unit cell parameters were determined as $a = 33.5$ nm and $c = 34.2$ nm with a close c/a ratio of ~1.02. Therefore, the first peak in its SAXS pattern was indexed to the 011 reflection of a tetragonal crystal, which is forbidden with the cubic G structure. Moreover, the strongest reflection at $q = 0.046$ Å⁻¹, which was comparable to the 112 reflection of cubic G, actually arose from overlap of the 112 and 211/121 reflections as a result of the nonequivalent (112) and (211) lattice planes in symmetry-reduced tetragonal crystals. Correspondingly, the neighboring shoulder peaks were indexed to the 022 and 220 reflections, respectively.

The pore shapes and sizes of cubic G and shifted tG were analyzed with N₂ adsorption-desorption isotherms (Figure S8). Both samples showed typical type-IV isotherms with evident hysteresis loops in the P/P₀ range of 0.4–0.9. The presence of an H1 hysteresis loop for cubic G indicated channel-type mesopores generated by the block copolymer template, whereas shifted tG showed a combination of H1- and H4-type hysteresis loops; this indicated the presence of both channel-type and narrow-slit-type mesopores, which could be attributed to the formation of slit mesopores by C₁₆TAB intercalated into the thinned silica matrix. The Brunauer-Emmett-Teller (BET) surface areas of cubic G and shifted tG were measured as 607.7 and 546.9 m² g⁻¹, respectively. The single-point total pore volume and mesopore volume determined by the α -plot method were 0.965 and 0.566 cm³ g⁻¹, respectively, for cubic G and 0.826 and 0.599 cm³ g⁻¹, respectively, for shifted tG. The pore diameters for cubic G and shifted tG were obtained by non-local density function theory (NLDFT) as ~10.5 and ~12.0 nm, respectively. These results indicate the high mesoporosity of both cubic G and shifted tG; however, the different isotherms suggested that their porous structure underwent significant changes.

It is worth noting that it is challenging to solve these structures solely by diffraction techniques because of their local fluctuations and surface roughness. Therefore, the structural details of the two samples were revealed by electron crystallography, which allows the direct visualization of the real space structures while retaining the phase information of crystal structure factors.^{56,57} Figures 1B–1D show the TEM images and the corresponding Fourier diffractograms (FDs) for cubic G taken from the [111], [001], and [110] directions, respectively. The extinction conditions { hkl : $h + k + l = 2n$ }, { $0kl$: $k = 2n$, $l = 2n$ }, { hhl : $2h + l = 4n$, $l = 2n$ }, and { $00l$: $l = 4n$ } obtained from the FDs were characteristic of the unique space-group symmetry *I*4̄3*d* (no. 230). The unit cell parameter $a \approx 34$ nm calculated from the FDs was consistent with the SAXS results. According to the symmetry-averaged TEM images obtained by the crystallographic image-processing software CRISP,⁵⁸ the typical two-dimensional (2D) plane groups of *p*6*mm*, *p*4*mm*, and *c*2*mm* were identified. In particular, the white dots shown in the <111> axis (Figure 1B) corresponded to the straight channels encircling the hexagonally organized G surface, which is considered a typical feature of cubic double-G surfaces.⁵⁹

In contrast, the diminished symmetry in shifted tG resulted in more intricate structural features. The low-magnification TEM images revealed the spherical

morphology of shifted tG with a size distribution statistical maximum of ~ 225 nm ([Figures S9–S11](#)). Representative detailed high-magnification TEM images from five different crystal orientations are shown in [Figures 1E–1I](#). The extinction conditions from FDs can be summarized as $\{hkl: h + k + l = 2n\}$, $\{hk0: h = 2n, k = 2n\}$, $\{0kl: k + l = 2n\}$, $\{hhl: l = 2n\}$, $\{0k0: k = 2n\}$, and $\{00l: l = 4n\}$ and are coincident with those of the unique space group $I4_1/a$ (no. 88). The lattice parameters determined from the FDs ($a \approx 33$ nm and $c \approx 1.02a$) agreed with the SAXS analysis. As a result of symmetry breaking, certain equivalent crystal orientations of cubic crystals become nonequivalent in tetragonal crystals. Differentiation of $\langle 111 \rangle_{\text{cub}}$, $\langle 001 \rangle_{\text{cub}}$, and $\langle 110 \rangle_{\text{cub}}$ orientations from the corresponding axes of cubic G to shifted tG are illustrated by colored lines with arrows in [Figure 1](#). Notably, as indicated by the red line pointing from [Figure 1B](#) to [Figure 1E](#), the 6-fold symmetry from the $\langle 111 \rangle_{\text{cub}}$ axis of cubic G was replaced by the 2-fold axis with the emergence of the 011 diffraction spot in FD, and the extra-dark contrasts beneath each white dot around the straight channels (marked by black arrows in [Figure 1E](#)) implied an unusual structural variation. As a result, the plane-group symmetry of the $[11\bar{1}]_{\text{tetra}}$ axis was lowered to p2. Similar variations were observed for the $[001]_{\text{tetra}}$ ([Figure 1F](#)) and $[010]_{\text{tetra}}$ ([Figure 1G](#)) axes of shifted tG, which are derived from the common $\langle 001 \rangle_{\text{cub}}$ axis of cubic G (indicated by blue lines pointing from [Figure 1C](#) to [Figures 1F and 1G](#)). Interestingly, the TEM image taken from the $[001]_{\text{tetra}}$ direction of shifted tG possessed the 4-fold symmetry ([Figure 1F](#)) with the plane group p4, whereas the $[010]_{\text{tetra}}$ direction exhibited c2mm symmetry with different TEM contrast. In addition, the $[110]_{\text{tetra}}$ ([Figure 1H](#)) and $[101]_{\text{tetra}}$ ([Figure 1I](#)) axes corresponded to the original $\langle 110 \rangle_{\text{cub}}$ direction are indicated by the green lines extending from [Figure 1D](#) to 1H and to 1I. Both directions exhibited the plane-group symmetry of p2mg, indicating the symmetry change from the original c2mm plane group of $\langle 110 \rangle_{\text{cub}}$. These results suggest the breaking of the original cubic symmetry and that only one of the 4-fold axes along $\langle 001 \rangle_{\text{cub}}$ was retained. These led to a structural transition from cubic to tetragonal; therefore, the $[001]_{\text{tetra}}$ became the unique axis in shifted tG.

3D structure reconstructions were used to reveal the configuration of the new structure. To reconstruct, we calculated the electrostatic potential maps of the two structures after extracting the structure factor phases and amplitudes out of the FDs obtained from their representative TEM images. Each 2D projection was unified to a common origin. For the shifted tG structure, the origin was chosen to be the inversion center (origin choice 2 of $I4_1/a$). We then merged the structure factor phases and amplitudes into one dataset upon scaling the common reflections and then corrected the amplitudes by the TEM contrast transfer function by using a Wiener filter to avoid division by zero. Finally, we generated the 3D electrostatic potential distributions $\varphi(x,y,z)$ via Fourier synthesis by employing the structure factors shown in [Tables S4](#) and [S5](#). The threshold values for the equi-electrostatic potential surfaces were set to 66% for cubic G and 68% for shifted tG out of the rescaled 0%–100%, which were determined by the mesopore volumes calculated from N_2 adsorption-desorption data. The pore size measured in the reconstructed volume is also consistent with the ~ 10.5 and ~ 12.0 nm pore sizes for cubic G and shifted tG, respectively, obtained from N_2 adsorption-desorption measurements ([Figure S12](#)).

The reconstructed electrostatic potential distribution for cubic G is shown in [Figure 2A](#). The G surface was replicated by uniform silica matrices ([Figures 2B](#) and [2D](#)). The embedded skeleton graphs representing the channel arrangements ([Figures 2C](#) and [2E](#)) indicated the three-coordinate interpenetrating double-gyroidal networks that divided the space in half, which resembled the conventional G

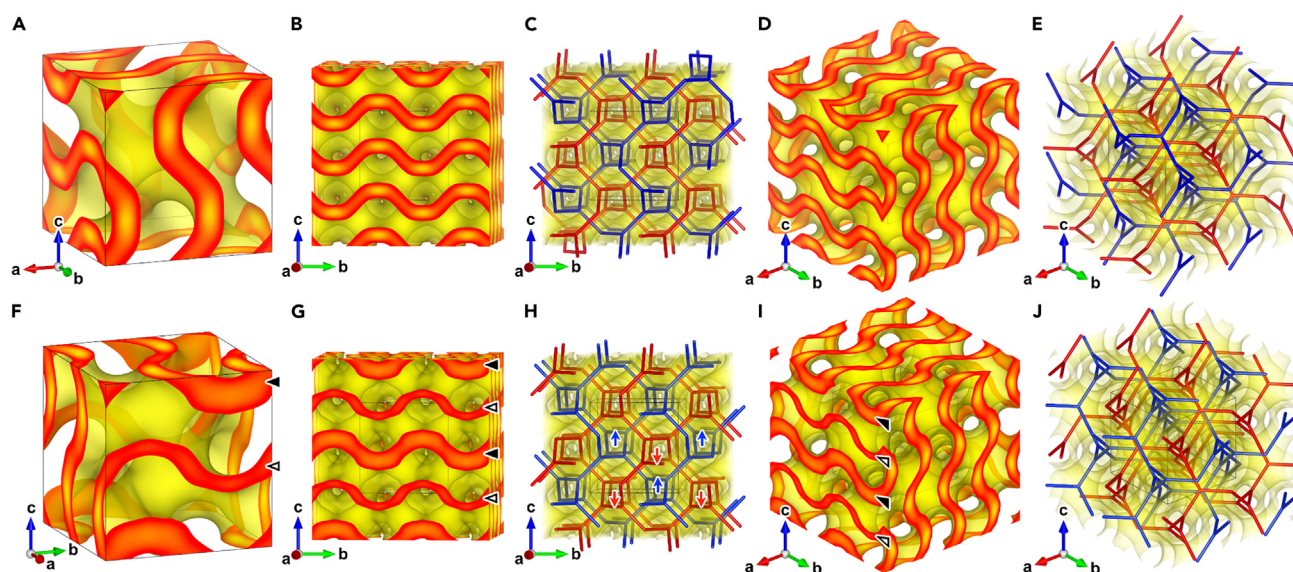


Figure 2. Reconstructed 3D electrostatic potential maps of cubic G and shifted tG

(A) Reconstructed unit cell of the cubic G structure.

(B–E) Electrostatic potential maps of cubic G (plot region: –0.5 to 1.5 unit cells); the skeleton graphs superimposed in the hollow channels are taken from near the [100] axis (B and C) and near the [111] direction (D and E).

(F) Reconstructed unit cell of the shifted tG structure.

(G–J) Electrostatic potential maps of shifted tG (plot region: –0.5 to 1.5 unit cells); the embedded skeleton graphs in the hollow channels are taken near the [100] axis (G and H) and near the [111] direction (I and J). The maps suggest an uneven silica matrix thickness along with shifted double channels with inverse helicity in the shifted tG structure. The solid and hollow triangles indicate the uneven matrix thickness, and the blue and red arrows suggest the azimuthally shifted frameworks.

surface as reported previously.^{60,61} The reconstructed unit cell of shifted tG was similar to that of cubic G at first glance (Figure 2F). However, we were surprised to find that the silica matrix of shifted tG was characterized by periodically distributed uneven wall thicknesses (indicated by alternating solid and hollow arrowheads). Correspondingly, the two networks were azimuthally shifted along the [001]_{tetra} axis by approximately 5% of the unit cell length of the c axis in comparison with cubic G. Therefore, the original 4-fold symmetry of cubic G was retained only along the unique axis [001]_{tetra} in shifted tG, as TEM investigations revealed. The projections from each direction are shown in Figure S13 and are consistent with the experimental images. To further verify the reconstructed 3D structure, we shot a series of tilted TEM images taken from one typical particle under different goniometer orientations in TEM observation (Figure 3). From the tilting sequence $\overline{[111]} \rightarrow \overline{[153]} \rightarrow \overline{[0\bar{1}\bar{1}]} \rightarrow \overline{[135]} \rightarrow \overline{[111]}$, the additional contrasts corresponding to the shifts of frameworks were highly consistent with the projections of the reconstructed structure in Figure 2, which fully confirmed the azimuthal displacements of the networks in shifted tG revealed by the structural solutions.

The distinctive structural features of shifted tG over cubic G are reflected not only in wall-thickness variations but also in the pore-shape inhomogeneities. For a better comparison, 2D sectional views of the reconstructed electrostatic potential maps for cubic G and shifted tG are displayed in Figure 4. The cross sections were taken at different fractional positions with respect to the d-spacing of the $\{hkl\}$ lattice planes. Unlike the conventional highly symmetric cubic G, shifted tG is characterized by asymmetrical electrostatic potential distributions, as indicated by the alternating solid triangles (indicating the thick matrix) and hollow triangles (indicating the thin matrix) in Figure 4B. These asymmetrical distributions manifested the variable

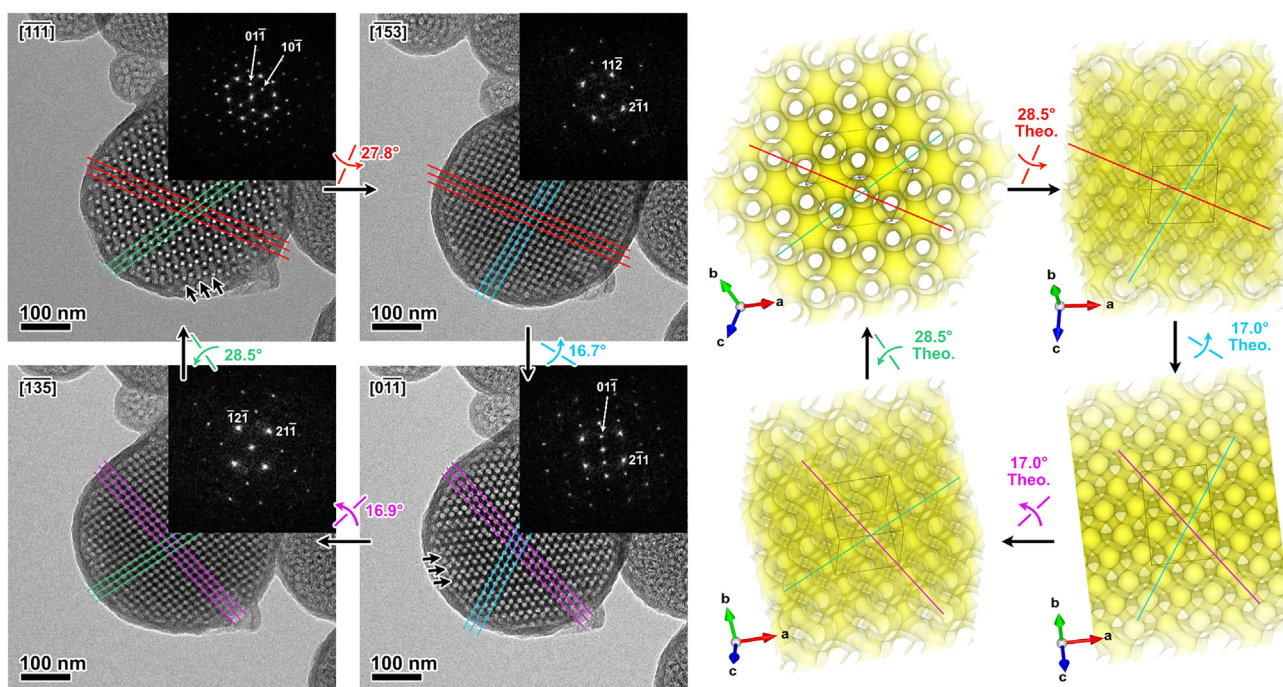


Figure 3. TEM images and the corresponding FDs of the tilting series from one typical particle of shifted tG taken from different orientations
The arrows indicate the directions and tilting angles of the goniometer axis. Parallel lines of the same color represent the lattice planes maintained during the tilting process. The projected electrostatic potential map and the theoretical tilting angles are shown on the right side.

pore shapes in shifted tG, which is another important factor that contributed to the formation of a lower-symmetry tetragonal structure. The full cross-sectional views of both cubic G and shifted tG from all corresponding directions are supplied in Figures S14 and S15, respectively.

Exploring the formation mechanism for shifted tG

It has been reported that during the microphase separation of diblock copolymer melts, the formation of TPMSs is favored when the volume fraction of the hydrophilic segments is in the range of 4%–14.1% vol.⁶² In this respect, our main building block PS₉₂-*b*-PAA₁₆ (volume fraction 10.5% for the PAA block) has a wide window for generating bicontinuous structures through phase separation. Given that the G structures with cubic symmetry were the only stable G phase in the former single-diblock-copolymer-assembled systems,¹⁴ the newly appeared shifted tG with a low-symmetry tetragonal lattice by symmetry breaking will suggest a fascinating formation mechanism for investigation.

Exploration of the formation mechanism of the unusual shifted tG structure begins with the debate over whether this structure is a thermodynamically stable mesophase or just a kinetically stable transition intermediate during the formation path of the cubic G structure, which was occasionally fossilized by silica species. To clarify this, we investigated the structure of the C₁₆TAB/PS₉₂-*b*-PAA₁₆ assemblies before the addition of inorganic precursors. We performed the TEM investigations of the pure C₁₆TAB/PS₉₂-*b*-PAA₁₆ composite micelles by directly dispersing the as-synthesized solution onto the microgrid and stained under RuO₄ vapor so that the PAA microdomains could be enhanced in TEM contrast. In the absence of C₁₆TAB, pure PS₉₂-*b*-PAA₁₆ produced only spherical particles around 50 nm in solvent/poor solvent mixture, whereas larger assembles were formed in the presence of C₁₆TAB.

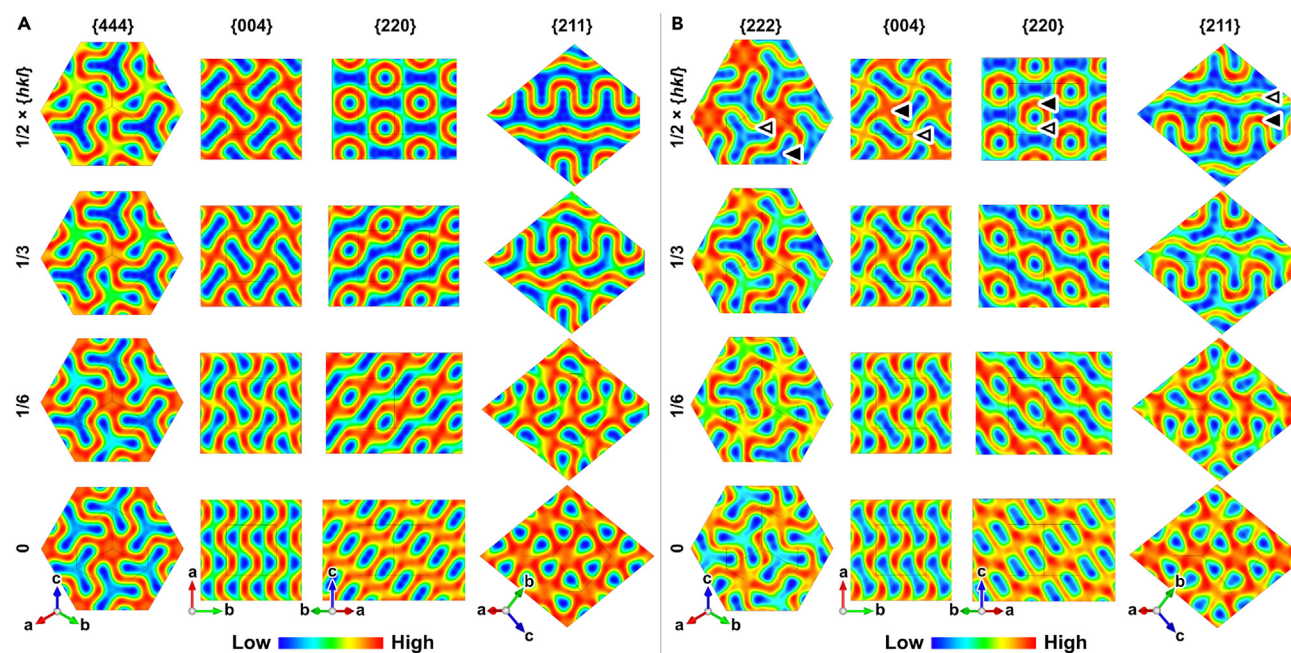


Figure 4. Slice view of 2D electrostatic potential maps of cubic G and shifted tG from representative directions

(A) Sliced 2D electrostatic potential of cubic G from the {444}, {004}, {220}, and {211} planes.

(B) Sliced 2D electrostatic potential of shifted tG from the {222}, {004}, {220}, and {211} planes.

We obtained the slices by cutting the reconstructed 3D volume from different orientations at a fraction of the d-spacing of the {hk\ell} planes, specified as an offset × {hk\ell}, to indicate the relative position of the slice with respect to the unit cell origin. Colors represent the electrostatic potential distribution values.

(Figure S16). Although the exact structure could not be totally resolved, the ordered lattice fringes shown in Figure S16C indicated that the structures were already formed before the addition of inorganic species. We then tried to dispel the suspicion that the shifted structure might not be formed by the self-assembly of the binary system of C₁₆TAB/PS₉₂-*b*-PAA₁₆ with silica precursors but by an accidental event due to calcination. As shown in Figure S17, both the SAXS measurement and the TEM observations confirmed that the shifted tG structure appeared in the as-synthesized sample before calcination, suggesting that the structure was direct related to the self-assembly process.

We further explored the thermodynamic stability of C₁₆TAB/PS₉₂-*b*-PAA₁₆ composite micelles by monitoring the influence of different incubation times on the final mesostructures (Figures S18 and S19). Because the incubation process happened before silica replication and there was no inorganic precursor during the incubation period, the composite micellar assemblies composed of the PS₉₂-*b*-PAA₁₆ and C₁₆TAB micelles could have undergone fusing, molecular rearranging, and/or the structural transformation toward the final equilibrium state. The morphological and structural transformations over time are therefore a key factor in revealing the thermodynamic stability of C₁₆TAB/PS₉₂-*b*-PAA₁₆ composite micelles. The sample synthesized with an incubation time of 0 min showed a lower degree of ordering because of the lack of sufficient equilibration time after C₁₆TAB and PS₉₂-*b*-PAA₁₆ were mixed. However, we can still recognize the typical contrast of the shifted tG structure from the TEM image (Figure S18A) and the characteristic 011 reflection of shifted tG in the SAXS pattern (Figure S19A). With extended equilibrium periods, the ordering of the structures was improved, and all samples maintained the shifted

tG structure known from both TEM observations and SAXS profiles. Notably, for the samples synthesized with longer incubation periods of 12 or 24 h, larger particles with shifted tG structure were formed as a result of fusion of the composite micellar assemblies. Therefore, it can be concluded that the formation of shifted tG is independent of the incubation period, and it should be a thermodynamically favored self-assembly process instead of a kinetically intermediate phase, which is highly associated with the periodic distribution of the PAA segment given the co-assembly behavior of PS₉₂-*b*-PAA₁₆ and C₁₆TAB.

The usage of C₁₆TAB was a crucial step in the synthesis process in that it could bring about a variety of interactions that offered a great deal of flexibility and controllability in regulating the self-assembly behaviors of block copolymers. We calculated the critical micelle concentration of C₁₆TAB at 35°C in our synthesis system as 0.95 mmol/L by employing pyrene fluorescence probe spectrometry ([Figure S20](#)). Therefore, the highly concentrated C₁₆TAB (13.7 and 17.1 mmol/L for the synthesis mixture of shifted tG and cubic G samples, respectively) joined the synthesis process in a micellar state. After the C₁₆TAB and PS₉₂-*b*-PAA₁₆ solutions were mixed, the C₁₆TAB micelles were incorporated in the PAA microdomain, as suggested by the N₂ adsorption-desorption results and the high-resolution TEM (HRTEM) observations of the mesopores in the silica wall region associated with the PAA segments ([Figure S21](#)). In order to gain a deeper understanding of role of auxiliary surfactant during the assembling process, we further investigated the effect of hydrophobic alkyl chain length on the evolution of structural geometry by employing the different cationic surfactant C_nTAB (n = alkyl chain length; see [Figures S22–S25](#) for details). It is worth noting that for tetradecyltrimethylammonium bromide (C₁₄TAB), a transition from disordered structure to shifted tG to cubic G was observed as the C₁₄TAB/PS₉₂-*b*-PAA₁₆ molar ratio increased. However, for octadecyltrimethylammonium bromide (C₁₈TAB), the lamellar structure formed with a low C₁₈TAB/PS₉₂-*b*-PAA₁₆ ratio directly transformed into cubic G after a lamellar/cubic G co-existing intermediate phase transition at a higher C₁₈TAB/PS₉₂-*b*-PAA₁₆ molar ratio. The synthesis-field diagram of the structures obtained from different addition amounts of C_nTAB molecules is summarized in [Figure 5A](#).

On the basis of these results, the effect of C_nTAB can be interpreted from the following two perspectives:

(1) The competition mechanism: In an aqueous self-assembled system, the structural geometries of micellar aggregates are determined by the packing parameter $p = V/a_0l$,⁶³ where V is the hydrophobic chain volume, a_0 is the molecular area of the hydrophilic head group, and l is the dynamical chain length. The ideal molecular shape in the p parameter qualitatively determines the spontaneous interfacial curvature of the corresponding micelles. The relation between p and the curvature is monotone: as the p parameter decreases, the interfacial curvature increases. TPMSs (including G structures) are usually formed with p values of 2/3 between the lamellar ($p = 1$) and cylindrical phases ($p = 1/2$).⁴ The effective p parameter will be influenced by a number of factors.⁵³ In the current scenario, C_nTAB affects the p parameter of the C_nTBA/PS₉₂-*b*-PAA₁₆ composite micelle in two possible ways: the insertion of C_nTAB micelles enlarges the head group and decreases the p parameter ([Figures 5B and 5C](#)), and the positively charged C_nTAB micelles tightly bind with the negatively charged acidic sites of PAA and lead to more compact but less entangled aggregates,^{64,65} leading to an increased packing parameter with lower interfacial curvature ([Figures 5B–5D](#)). The interplay of these two opposing factors determines the final organization

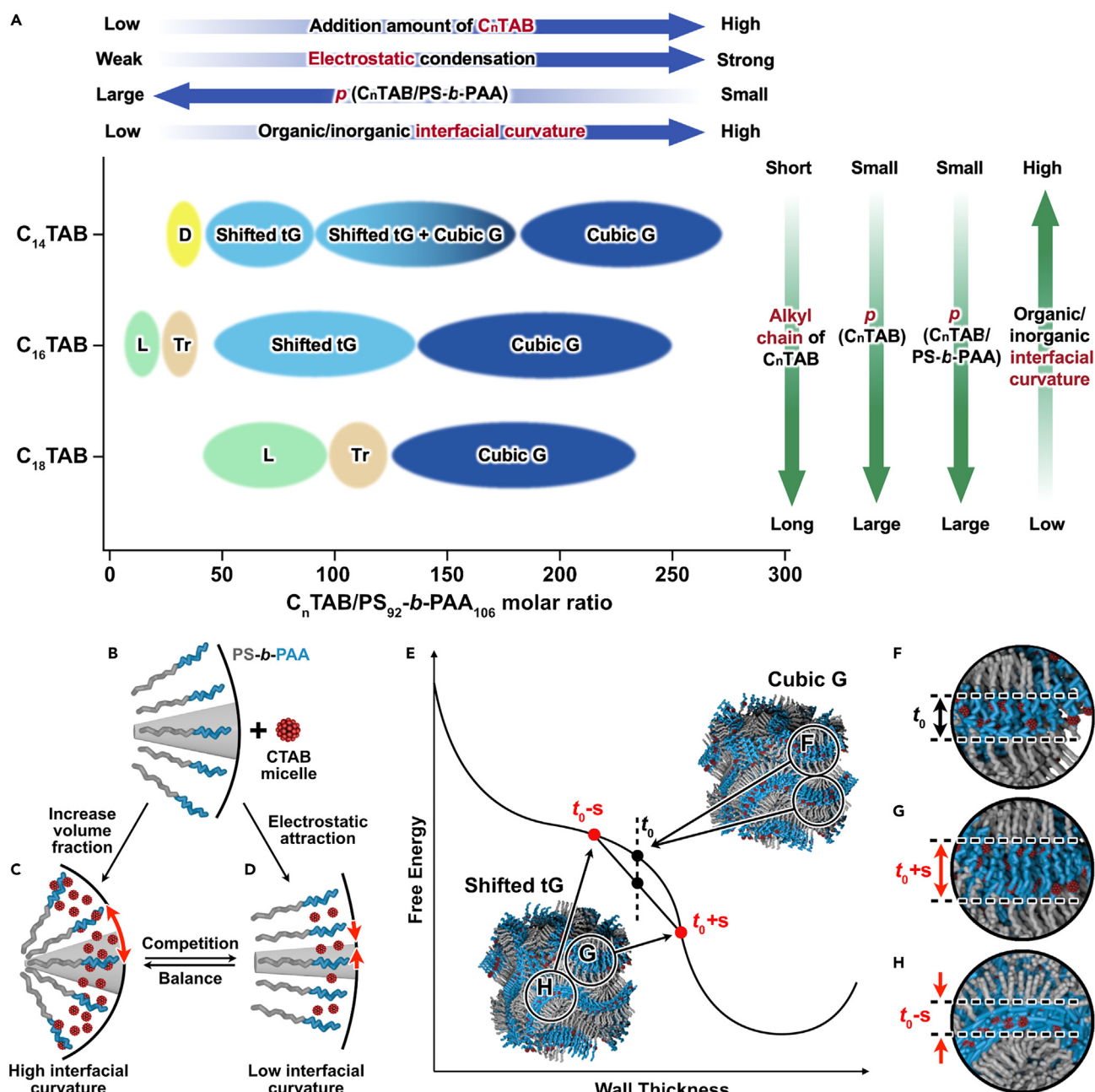


Figure 5. Synthesis-field diagram and schematic drawing of the geometrical changes and corresponding molecular arrangements in the cubic G and shifted tG structures

(A) Synthesis-field diagram of the mesostructures obtained by different C_n TAB molecules. The disordered (D), lamellar (L), transition intermediate from lamellar to 3D structure (Tr), and shifted tG and cubic G structures were obtained.

(B-D) The tuning of packing parameter upon the addition of C_n TAB.

(E) The changes of free energies and the corresponding molecular arrangements in the cubic G and shifted tG structures. The free energy can be reduced as a function of the wall thickness (degree of molecular curling). Cubic G with a uniform wall thickness is replaced by shifted tG with decreased global free energy.

(F-H) Enlarged views of the arrangement of PAA chains shown in (E).

of the co-micelles. With a small amount of C_n TAB, the C_n TAB micelles might be located in the interstitial spaces of the polymer chain and contribute less to the volume fraction. But the electrostatic interaction would induce the compression

of PAA segment to form a loose lamellar-like structure with low interfacial curvature ([Figure 5D](#)). In contrast, the insertion of a large amount of C_nTAB would greatly increase the volume fraction of hydrophilic species and serve as a major factor influencing the geometry ([Figure 5C](#)).

(2) The curvature matching effect: The geometrical relationship between the C_nTAB micelles and the PS₉₂-b-PAA₁₆ during the formation of composite micelles also contributes to the structural formations. Known from the synthesis-field diagram, under a similar synthetic molar ratio, the transition from C₁₄TAB to C₁₈TAB increases the ρ parameter of the composite micelles (indicated by the green vertical arrows from top to bottom in the synthesis-field diagram). It is interesting that the composite co-micelle tends to adopt a lower-curvature structure (such as lamellar) coincident with the presence of low-curvature C_nTAB micelles (the longer the alkyl chain lengths, the higher the g parameter and the lower the micellar curvature). As shown in the TEM images of C₁₈TAB ([Figure S24B](#)), in the midst of large pores in the lamellar cocoon-type particles, intriguing multilayered structures were formed by the templating effect of inserted lamellar C₁₈TAB micellar assemblies (C₁₈TAB with long alkyl tails prefer the lamellar micelle), suggesting that the morphology and the geometry of the C_nTAB micelles greatly influence the final structures of the composite co-micelle. Therefore, it can be speculated that for a binary system with different auxiliary surfactants, the curvature matching between the C_nTAB micelle and the composite micelle plays a critical role in determining the final structure. This matching effect of the lamellar trends of C₁₈TAB micelles is so strong that we cannot obtain shifted tG in the C₁₈TAB system, and the lamellar structure still co-exists with the cubic G structure even in a high proportion of C₁₈TAB ([Figures S24D](#) and [S24E](#)). Notably, C₁₆TAB has the widest synthesis window for the ordered mesostructures, indicating that an appropriate alkyl chain length is beneficial to the matching of the two micelles.

The premise of the ρ parameter theory assumes ideal shapes and organizations of polymer chains, but the actual organization in real synthesis systems is much more complicated. The alternating thickness of the walls in shifted tG, which is the main contrast between shifted tG and cubic G, can not be fully explained by the ρ parameter or the curvature predicated by the ρ parameter. Notably, shifted tG occurred only under an intermediate proportion of C₁₄TAB and C₁₆TAB. We considered the formation of shifted tG from the perspective of energy distribution. As revealed by the 3D reconstructed electrostatic potential map, the unshifted cubic G structure has a uniform matrix (silica wall) thickness assumed to be t_0 , whereas the uneven matrix thickness in shifted G decreased by s for the thinner walls ($t_{\text{thin}} = t_0 - s$) and increased by the same amount for the thicker walls ($t_{\text{thick}} = t_0 + s$) as symmetrical correspondence. According to the aforementioned analysis, the shifted tetragonal G structure was formed under thermodynamic equilibrium driven by energy minimization. When we consider the local free energy $g(t)$ as a black-box function of the local wall thickness t , t_0 is necessarily not a local minimizer of $g(t)$. To meet the demands of minimized local free energy, there must be a condition of $g(t_0 - s) + g(t_0 + s) < 2g(t_0)$. In other words, the local free energy $g(t)$ is a concave function around $t = t_0$, and only then is there an actual decrease in the global free energy for shifted tG, which is obtained by integration of $g(t)$ along the surface ([Figure 5E](#)). Therefore, the shifted tG structure can be considered experimental evidence for the local concaveness theory of the local free energy, and the degree of shifting gives us a rough idea of the size of the concave region.

This local concaveness of the local free energy in shifted tG should be traced back to the molecular organization. In a recent report, the degree of freedom, including the molecular tilting or twisting of the building blocks, significantly affects the free

energy of the self-assembly of bicontinuous structures and is highly related to the thickness of the bilayers.⁶⁶ For microphase separation of block copolymers, the stability of the phases depends not only on the volume fraction but also critically on the polymer chain structure and conformational rigidity, thus exhibiting a variation in matrix thickness at an almost constant molecular density.⁶⁷ According to this theory, the local concaveness in our current binary-assembly synthetic system could be considered evidence of the molecular stretching or curling of PS₉₂-*b*-PAA₁₆, which would be the direct cause of the thickness variation in shifted tG. In this aspect, cubic G shows a medial matrix thickness (Figure 5F), whereas the stretching of the PAA segment in shifted tG results in a thicker matrix (Figure 5G) and the polymeric curling leads to the compression of the PAA chain, corresponding to a thinner wall (Figure 5H). We speculate that a delicate equilibrium can be reached with the appropriate amount of C_nTAB so as to generate a lower overall free energy, and this configuration can be achieved only in the binary system, whereas the C_nTAB additive is the key factor for relaxing the constraint of volume balancing of the matrix by redistributing the cost of packing frustration. Conversely, in the situation of cubic G, the larger amount of inserted C_nTAB renders more tightly bound PAA chains and thus greatly hinders tilting or twisting; hence, a wall of uniform thickness is formed. Therefore, the alternating wall thickness (the critical point that directly induces the shifted tG with broken symmetry) appears only within a specific C_nTAB/PS₉₂-*b*-PAA₁₆ molar ratio just right between lamellar and cubic G.

In addition, the appearance of shifted tG could also be considered experimental evidence of the theoretical prediction of the tetragonal deformations of G to the diamond (D) surface proposed before.^{49,50} In this kind of deformation, the tetragonal deformation of the D surface generated the tetragonal G structure with the space group I4₁/acd by keeping the surface minimal and maintaining its integrity all through different ratios of the *c/a* lattice parameters. This tetragonal deformation pathway was supported by the orientational relationship in the D → G transition in the lyotropic liquid crystal phases of lipids.^{68,69} Unfortunately, this liquid crystalline tetragonal G has not yet been practically confirmed. It is worth noting that although neither the D structure nor the D → G transition was observed in the current syntheses, the validation of shifted tG suggested that the tetragonal deformation of cubic G to shifted tG might not be a simple crystal compression or stretching pathway but might instead be accompanied by an azimuthal shift and deformation of the network to achieve energetic optimization.

Calculation of the optical properties of shifted tG

Bicontinuous structures have long been considered a candidate pool for building 3D photonic crystals. However, the cubic double G cannot generate a photonic band gap as a result of its increased symmetry. Therefore, to explore new possibilities for opening up the photonic band gap in G structures, it is necessary to investigate the effects of labyrinths shifting from the cubic G to shifted tG structures on the evolution of optical properties.

We studied the propagation of the electromagnetic waves within shifted G by numerically solving Maxwell's equation by using the MIT Photonic-Bands package.⁷⁰ The approximate structural model was built by the level surface function:

$$\sin(2\pi x)\cos(2\pi y) + \sin(2\pi y)\cos(2\pi z) + \sin(2\pi z)\cos(2\pi x) = t,$$

where *t* is the threshold value that determines the pore volume fraction. Here, the volume fraction of each pore channel was set to 30%, and the volume fraction of the wall matrix was 40% according to the reconstructed volume fraction. The lower

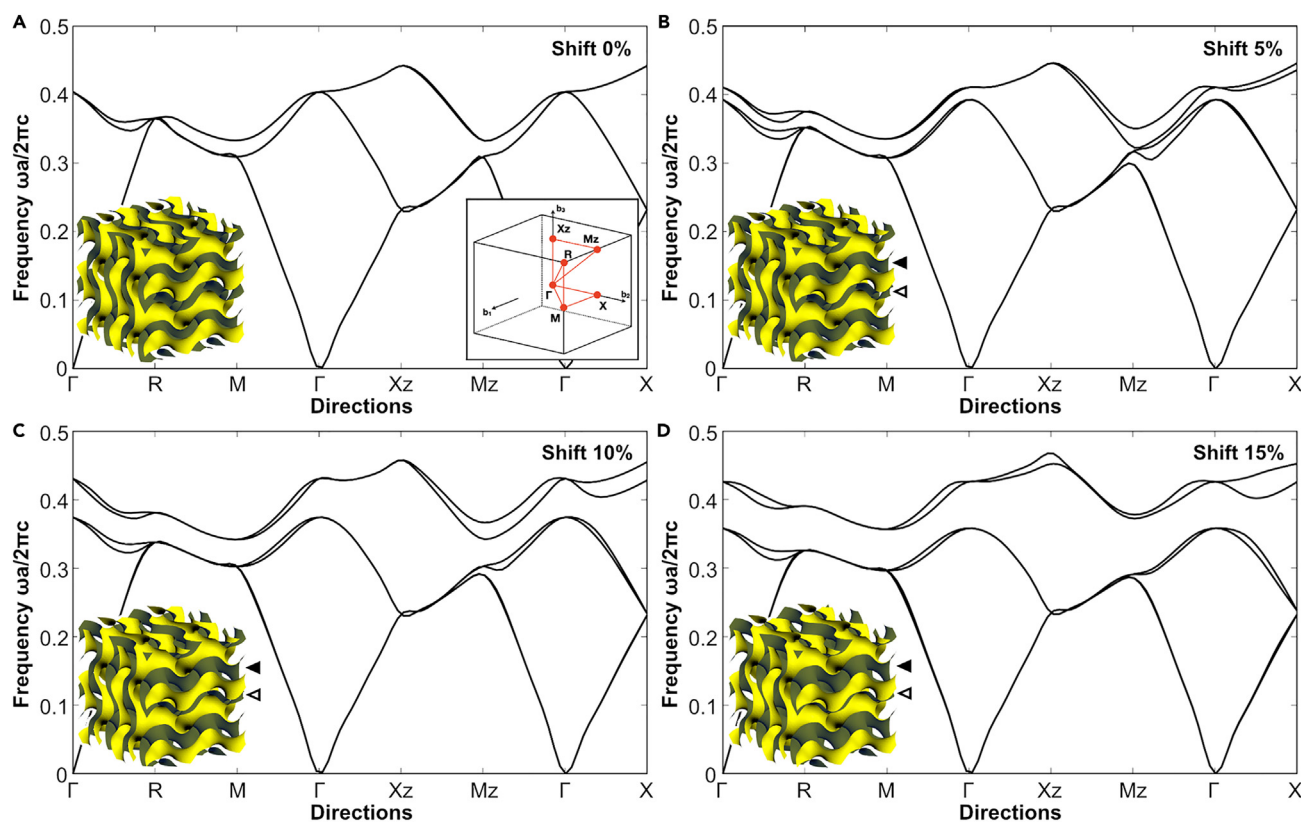


Figure 6. The band structures of cubic G and shifted tG with different shift values

- (A) The band structure of cubic G.
(B) The band structure of shifted tG with a shift value of 5% for the c axis.
(C) The band structure of shifted tG with a shift value of 10% for the c axis.
(D) The band structure of shifted tG with a shift value of 15% for the c axis.
The insets show the corresponding structural models and Brillouin zones used for calculating the band structure.

dielectric material was set as air with $\epsilon_1 = 1$, and the higher dielectric material was assumed to have $\epsilon_2 = 13$. The Brillouin zone was embedded in a modified cubic lattice to incorporate the unique directions in the tetragonal lattice. As shown in Figure 6, shifting the frameworks along the [001] axis gradually opened a new photonic band gap, and the band-gap width increased as the shifting degree was enhanced. However, it is difficult to obtain a complete band gap from a tetragonal G with the current volume fraction setting because networks begin to fuse into a single G at a shift value above 15% for the c axis. Nevertheless, the opening up of the band gap based on the cubic-to-tetragonal symmetry transition offers a new avenue for designing novel optical materials and indicates the potential of shifted tG for future functional optical materials.

Conclusions

In conclusion, we have experimentally discovered a subphase of the G structure (shifted tG) in a binary self-assembly system containing block copolymer PS₉₂-*b*-PAA₁₆ and modulating surfactant C₁₆TAB. Using meticulous electron crystallographic structural studies, we determined this structure to be a tetragonal G structure with an unevenly distributed silica wall matrix and two skeletons shifted along the [001] axis relative to those of cubic G and associated with the lower-symmetry space group *I*4₁/a. The shifted tG and cubic G structures exhibited similarities that created challenges in distinguishing the obtained structures, which might require

extreme caution in avoiding erroneous structural assignments in further TPMS studies. The formation of shifted tG was interpreted by the alternating organization of molecular stretching or curling of the block copolymer in the cooperative self-assembly induced by C₁₆TAB, which favored the generation of a lower overall free energy. The transition from cubic to tetragonal symmetry created a new photonic band gap that is not feasible with a cubic double-G structure. Our report could open up new avenues for generating more novel functional materials with peculiar properties on the basis of manipulating the symmetry of the G surface family and other hyperbolic surface species. This work provides a fresh impetus for enriching the bicontinuous family and generating a deeper understanding of the hyperbolic surfaces and thus exhibits potential for straightforward structural distorting and deforming strategies for exploring additional chemical and material science applications.

EXPERIMENTAL PROCEDURES

Resource availability

Lead contact

Requests for further information and resources should be directed to and will be fulfilled by the lead contact, Lu Han (luhan@tongji.edu.cn).

Materials availability

All reagents associated with this study either are commercially available or can be easily prepared as described in the [supplemental information](#).

Data and code availability

All data supporting this study are available in the main text or the [supplemental information](#). Any additional information required for reanalyzing the data reported in this paper is available from the [lead contact](#) upon request.

Chemicals

Tetraethyl orthosilicate (TEOS, equivalent SiO₂, ≥28%) and toluene (≥99.5%) were purchased from Sinopharm Chemical Reagent. The ammonia solution (25%–28%), tetrahydrofuran (THF, ≥99.5%), dichloromethane (DCM, ≥99.5%), methanol (≥99.5%), trifluoroacetic acid (TFA, ≥99%), and ethanol (≥99.8%) were obtained from Shanghai Titan Scientific. Cetyltrimethylammonium bromide (C₁₆TAB, ≥99%), octadecyltrimethylammonium bromide (C₁₈TAB, ≥98%), and cuprous bromide (CuBr, ≥99%) were purchased from Aladdin Holdings Group. Methyl 2-bromopropionate (MBP, ≥98%), N,N,N',N'',N'''-pentamethyldiethylenetriamine (PMDETA, ≥99%), tetradecyltrimethylammonium bromide (C₁₄TAB, ≥98%), t-butyl acrylate (t-BA, ≥98.0%), and styrene (St, ≥99.0%) were purchased from Tixaid (Shanghai) Chemical Industry Development. Water was purified with a Milli-Q system and had an electrical resistance of 18.2 MΩ·cm⁻¹. t-BA was purified by filtration through an Al₂O₃ column for removal of the polymerization inhibitor.

Synthesis of PtBA₁₆-Br

The macroinitiator PtBA₁₆-Br was synthesized by the well-established atom transfer radical polymerization (ATRP) technique with t-BA at 60°C and with MBP as the initiator and cuprous bromide/N,N,N',N'',N'''-pentamethyldiethylenetriamine (CuBr/PMDETA) as the catalyst system. Typically, MBP (0.308 mol, 5.150 g) was dissolved in 97 mL of toluene in a 250 mL Schlenk flask, and t-BA (0.400 mol, 58 mL), PMDETA (0.308 mol, 6.41 mL), and CuBr (0.308 mol, 4.418 g) were added to the solution. The reaction system was fully degassed with more than three freeze-pump-thaw cycles and sealed under vacuum. The bottle was then placed in an oil bath at 60°C so that polymerization could occur. After exposing the reaction mixture to air terminated the polymerization, the

catalyst was removed with filtration through an Al_2O_3 column with methylene chloride as the eluent. After rotary evaporation to remove the methylene chloride and toluene, the macroinitiator $\text{PtBA}_{16}\text{-Br}$ was obtained.

Synthesis of $\text{PS}_{92}\text{-}b\text{-}\text{PtBA}_{16}$

$\text{PS}_{92}\text{-}b\text{-}\text{PtBA}_{16}$ was synthesized by ATRP of St at 90°C with $\text{PtBA}_{16}\text{-Br}$ as the initiator and $\text{CuBr}/\text{PMDETA}$ as the catalyst system. A 250 mL Schlenk flask containing $\text{PtBA}_{16}\text{-Br}$ (4.31 mmol, 9.0 g), PMDETA (8.61 mmol, 1.79 mL), 65 mL of toluene, and 64.0 mL of St (0.557 mol) was purged thoroughly and then sealed with a rubber stopper. After the solution became clear with stirring in an ice-water bath, CuBr (4.31 mmol, 0.63 g) was added to the solution. The bottle containing the reactants was fully degassed with more than three freeze-pump-thaw cycles and sealed under vacuum. The flask was then placed in an oil bath at 90°C so that polymerization could occur. The reaction time was controlled at 6 h. After the reaction, as with the synthesis of $\text{PtBA}_{16}\text{-Br}$, the mixtures were cooled to room temperature, the catalyst was removed, and the block copolymer $\text{PS}_{92}\text{-}b\text{-}\text{PtBA}_{16}$ was finally obtained by precipitation with cold methanol (500 mL) after rotary evaporation.

Synthesis of $\text{PS}_{92}\text{-}b\text{-}\text{PAA}_{16}$

The amphiphilic copolymer $\text{PS}_{92}\text{-}b\text{-}\text{PAA}_{16}$ was hydrolyzed from $\text{PS}_{92}\text{-}b\text{-}\text{PtBA}_{16}$. $\text{PS}_{92}\text{-}b\text{-}\text{PtBA}_{16}$ (1.71 mmol, 20.0 g) was dissolved in 150 mL of DCM in a 250 mL beaker, and then 58.6 mL of trifluoroacetic acid (0.79 mol) was added to the mixture. The reaction was stirred at room temperature for 3 days. After rotary evaporation to remove most of the DCM, the concentrate was added to cold methanol to precipitate the $\text{PS}_{92}\text{-}b\text{-}\text{PAA}_{16}$ diblock copolymer, which was collected by filtration and dried under vacuum at room temperature.

Sample preparation

In a 35°C water bath, we prepared a copolymer solution (solution A) by dissolving 25 mg of block copolymer $\text{PS}_{92}\text{-}b\text{-}\text{PAA}_{16}$ in 5 mL of THF (5 mg/mL) and prepared a surfactant solution (solution B) by dissolving the surfactant C_{16}TAB (0.274 mmol, 100 mg) and 250 μL of ammonia in 20 mL of Milli-Q water (4 mg/mL). We prepared an inorganic precursor solution by dropwise adding 0.15 g of TEOS into 40 mL of ethanol. Then, solution A was quickly poured into solution B with rapid stirring (700 rpm) and stirred for another 2–3 s. After standing for 1 h, the mixture was diluted with the ethanol precursor solution of TEOS with continuous stirring for 10 min. The usage of the precursor solution granted an even dispersion and an appropriate hydrolysis rate of TEOS molecules as a result of the presence of ethanol. The reaction solution was then aged for 18 h. The as-synthesized nanoparticles were collected by centrifugation, washed with Milli-Q water and ethanol for several hours, and dried in a vacuum oven at 35°C for 12 h. Template-free samples were obtained by calcination of the as-made samples at 550°C for 6 h.

Characterizations

SAXS patterns were obtained on a Rigaku NANOPIX system. The X-ray generator was Fr-x (rotation anode X-ray generator) with a power of 2.97 kW (45 kV, 66 mA), and the λ for the target Cu source was 1.5406 Å. The camera length was 1,290 mm. The incident beam was from New CMF optics, and the detector was a Hy-Pix-54000. All ID profiles were collected with two-pinhole, high-resolution-type collimation with a beam stop size of 2.0 mm φ . Before measurements, the camera length was calibrated with silver behenate. The NMR spectra were recorded via a Bruker Avance 600 MHz NMR spectrometer using tetramethylsilane (TMS) as the internal reference. The nitrogen adsorption-desorption experiment was performed with Quantachrome Instruments Autosorb iQ at 77 K. All of the samples were degassed

under vacuum at 120°C for 3 h prior to analysis. The specific surface areas and the pore-size distribution were calculated with the BET and NLDFT methods, respectively. TEM experiments were performed with a JEOL JEM-F200 microscope equipped with a Schottky gun operating at 200 kV (Cs 1.0 mm, Cc 1.1 mm, point resolution of 1.9 Å for TEM). Images were recorded with a GATAN OneView IS camera (4,096 × 4,096 pixels) under low-dose conditions. For TEM observations, the samples were crushed, dispersed in ethanol, and dripped on a carbon thin film on a Cu grid.

SUPPLEMENTAL INFORMATION

Supplemental information can be found online at <https://doi.org/10.1016/j.chempr.2023.12.017>.

ACKNOWLEDGMENTS

The authors thank Prof. Hexiang Deng and Mr. Gaoli Hu at Wuhan University for helping with SAXS measurements. This work was financially supported by the National Key Research and Development Program of China (grant 2022YFC2403200 to Y.L. and Y.C.), the National Natural Science Foundation of China (grants 22005096 to Y.C., 51972112 to Y.L., and 22373074 to L.H.), the Key Field Research Program (grant 2023AB054 to Y.L.), the Basic Research Program of Shanghai (grant 21JC1406003 to Y.L.), the Shanghai Sailing Program (grant 20YF1410100 to Y.C.), and the Fundamental Research Funds for the Central Universities (granted to Y.C. and L.H.).

AUTHOR CONTRIBUTIONS

S.W. performed the synthesis and the basic characterizations of the samples under the supervision of Y.C. and Y.L.; L.H. solved the structure by electron crystallography and reconstructed the 3D electrostatic potential map; Q.D. contributed to the 3D reconstruction; H.C. calculated the photonic band gap; Y.C., L.H., H.C., and Y.L. contributed to the analysis of the formation mechanism; Y.C. prepared the draft of the manuscript, which was enriched by L.H., H.C., and Y.L.; and all authors contributed to the preparation of the final manuscript.

DECLARATION OF INTERESTS

The authors declare no competing interests.

Received: August 18, 2023

Revised: October 5, 2023

Accepted: December 18, 2023

Published: January 15, 2024

REFERENCES

1. Schoen, A. (1970). Infinite periodic minimal surfaces without self-intersections. National Aeronautics and Space Administration Technical Note (National Aeronautics and Space Administration), p. D-5541.
2. Andersson, S., Hyde, S.T., Larsson, K., and Lidin, S. (1988). Minimal surfaces and structures: from inorganic and metal crystals to cell membranes and biopolymers. *Chem. Rev.* 88, 221–242.
3. Grosse-Brauckmann, K. (1997). On gyroid Interfaces. *J. Colloid Interface Sci.* 187, 418–428.
4. Han, L., and Che, S. (2018). An overview of materials with triply periodic minimal surfaces and related geometry: from biological structures to self-assembled systems. *Adv. Mater.* 30, e1705708.
5. Qin, Z., Jung, G.S., Kang, M.J., and Buehler, M.J. (2017). The mechanics and design of a lightweight three-dimensional graphene assembly. *Sci. Adv.* 3, e1601536.
6. Kibsgaard, J., Chen, Z., Reinecke, B.N., and Jaramillo, T.F. (2012). Engineering the surface structure of MoS₂ to preferentially expose active edge sites for electrocatalysis. *Nat. Mater.* 11, 963–969.
7. Hsueh, H.Y., and Ho, R.M. (2012). Bicontinuous ceramics with high surface area from block copolymer templates. *Langmuir* 28, 8518–8529.
8. Robbins, S.W., Beaucage, P.A., Sai, H., Tan, K.W., Werner, J.G., Sethna, J.P., DiSalvo, F.J., Gruner, S.M., Van Dover, R.B.V., and Wiesner, U. (2016). Block copolymer self-assembly-directed synthesis of mesoporous gyroidal superconductors. *Sci. Adv.* 2, e1501119.
9. Beaucage, P.A., Dover, R.B. van, DiSalvo, F.J., Gruner, S.M., and Wiesner, U. (2021). Superconducting quantum metamaterials

- from convergence of soft and hard condensed matter science. *Adv. Mater.* 33, e2006975.
10. Crossland, E.J.W., Kamperman, M., Nedelcu, M., Ducati, C., Wiesner, U., Smilgies, D.M., Toombes, G.E.S., Hillmyer, M.A., Ludwigs, S., Steiner, U., et al. (2009). A bicontinuous double gyroid hybrid solar cell. *Nano Lett.* 9, 2807–2812.
 11. Hsueh, H.Y., Chen, H.Y., She, M.S., Chen, C.K., Ho, R.M., Gwo, S., Hasegawa, H., and Thomas, E.L. (2010). Inorganic gyroid with exceptionally low refractive index from block copolymer templating. *Nano Lett.* 10, 4994–5000.
 12. Goi, E., Cumming, B.P., and Gu, M. (2018). Gyroid “srs” networks: photonic materials beyond nature. *Adv. Opt. Mater.* 6, 1800485.
 13. Stefk, M., Guldin, S., Vignolini, S., Wiesner, U., and Steiner, U. (2015). Block copolymer self-assembly for nanophotonics. *Chem. Soc. Rev.* 44, 5076–5091.
 14. Park, H., Jo, S., Kang, B., Hur, K., Oh, S.S., Ryu, D.Y., and Lee, S. (2022). Block copolymer gyroids for nanophotonics: significance of lattice transformations. *Nanophotonics* 11, 2583–2615.
 15. Dolan, J.A., Wilts, B.D., Vignolini, S., Baumberg, J.J., Steiner, U., and Wilkinson, T.D. (2015). Optical properties of gyroid structured materials: from photonic crystals to metamaterials. *Adv. Opt. Mater.* 3, 12–32.
 16. Hyde, S.T., and Schröder-Turk, G.E. (2012). Geometry of interfaces: topological complexity in biology and materials. *Interface Focus* 2, 529–538.
 17. Almsherqi, Z.A., Landh, T., Kohlwein, S.D., and Deng, Y. (2009). Cubic membranes—the missing dimension of cell membrane organization. In *Int. Rev. Cell Mol. Biol.*, 274, pp. 275–342.
 18. Saranathan, V., Osuji, C.O., Mochrie, S.G.J., Noh, H., Narayanan, S., Sandy, A., Dufresne, E.R., and Prum, R.O. (2010). Structure, function, and self-assembly of single network gyroid ($I4132$) photonic crystals in butterfly wing scales. *Proc. Natl. Acad. Sci. USA* 107, 11676–11681.
 19. Wilts, B.D., Apeleo Zubiri, B.A., Klatt, M.A., Butz, B., Fischer, M.G., Kelly, S.T., Speecker, E., Steiner, U., and Schröder-Turk, G.E. (2017). Butterfly gyroid nanostructures as a time-frozen glimpse of intracellular membrane development. *Sci. Adv.* 3, e1603119.
 20. Ullal, C.K., Maldovan, M., Thomas, E.L., Chen, G., Han, Y.-J., and Yang, S. (2004). Photonic crystals through holographic lithography: simple cubic, diamond-like, and gyroid-like structures. *Appl. Phys. Lett.* 84, 5434–5436.
 21. Gan, Z., Turner, M.D., and Gu, M. (2016). Biomimetic gyroid nanostructures exceeding their natural origins. *Sci. Adv.* 2, e1600084.
 22. Peng, S., Zhang, R., Chen, V.H., Khabiboulline, E.T., Braun, P., and Atwater, H.A. (2016). Three-dimensional single gyroid photonic crystals with a mid-infrared bandgap. *ACS Photonics* 3, 1131–1137.
 23. Nowak, S.R., Lachmayr, K.K., Yager, K.G., and Sita, L.R. (2021). Stable thermotropic 3D and 2D double gyroid nanostructures with sub-2-nm feature size from scalable sugar-polyolefin conjugates. *Angew. Chem. Int. Ed.* 60, 8710–8716.
 24. Lu, H., Zeng, X., Ungar, G., Dressel, C., and Tschierske, C. (2018). The solution of the puzzle of smectic-Q: the phase structure and the origin of spontaneous chirality. *Angew. Chem. Int. Ed.* 57, 2835–2840.
 25. Chen, C., Kieffer, R., Ebert, H., Prehm, M., Zhang, R.B., Zeng, X., Liu, F., Ungar, G., and Tschierske, C. (2020). Chirality induction through nano-phase separation: alternating network gyroid phase by thermotropic self-assembly of X-shaped bolapolyphiles. *Angew. Chem. Int. Ed.* 59, 2725–2729.
 26. Luzzati, V., Tardieu, A., and Gulik-Krzywicki, T. (1968). Polymorphism of lipids. *Nature* 217, 1028–1030.
 27. Lynch, M.L., and Spicer, P.T. (2005). Bicontinuous Liquid Crystals (Taylor & Francis Group).
 28. Mezzenga, R., Seddon, J.M., Drummond, C.J., Boyd, B.J., Schröder-Turk, G.E., and Sagalowicz, L. (2019). Nature-inspired design and application of lipidic lyotropic liquid crystals. *Adv. Mater.* 31, e1900818.
 29. Hajduk, D.A., Harper, P.E., Gruner, S.M., Honeker, C.C., Kim, G., Thomas, E.L., and Fetter, L.J. (1994). The gyroid: a new equilibrium morphology in weakly segregated diblock copolymers. *Macromolecules* 27, 4063–4075.
 30. Matsen, M.W., and Schick, M. (1994). Stable and unstable phases of a diblock copolymer melt. *Phys. Rev. Lett.* 72, 2660–2663.
 31. Matsen, M.W. (1995). Stabilizing new morphologies by blending homopolymer with block copolymer. *Phys. Rev. Lett.* 74, 4225–4228.
 32. Bates, F.S., and Fredrickson, G.H. (1999). Block copolymers—designer soft materials. *Phys. Today* 52, 32–38.
 33. Xiang, L., Li, Q., Li, C., Yang, Q., Xu, F., and Mai, Y. (2023). Block copolymer self-assembly directed synthesis of porous materials with ordered bicontinuous structures and their potential applications. *Adv. Mater.* 35, e2207684.
 34. Llandro, J., Love, D.M., Kovács, A., Caron, J., Vyas, K.N., Kákay, A., Salikhov, R., Lenz, K., Fassbender, J., Scherer, M.R.J., et al. (2020). Visualizing magnetic structure in 3D nanoscale Ni–Fe gyroid networks. *Nano Lett.* 20, 3642–3650.
 35. Lv, H., Zheng, Y., Wang, Y., Wang, J., Liu, B., and Qiao, Z.A. (2023). Ordered mesoporous intermetallic Ga-Pt nanoparticles: phase-controlled synthesis and performance in oxygen reduction electrocatalysis. *Angew. Chem. Int. Ed.* 62, e202304420.
 36. Shefelbine, T.A., Vigild, M.E., Matsen, M.W., Hajduk, D.A., Hillmyer, M.A., Cussler, E.L., and Bates, F.S. (1999). Core–shell gyroid morphology in a poly(isoprene-block-styrene-block-dimethylsiloxane) triblock copolymer. *J. Am. Chem. Soc.* 121, 8457–8465.
 37. Hückstädt, H., Goldacker, T., Göpfert, A., and Abetz, V. (2000). Core–shell double gyroid morphologies in ABC triblock copolymers with different chain topologies. *Macromolecules* 33, 3757–3761.
 38. Epps, T.H., Cochran, E.W., Bailey, T.S., Waletzko, R.S., Hardy, C.M., and Bates, F.S. (2004). Ordered network phases in linear poly(isoprene-*b*-styrene-*b*-ethylene oxide) triblock copolymers. *Macromolecules* 37, 8325–8341.
 39. Wang, H.F., Chiu, P.T., Yang, C.Y., Xie, Z.H., Hung, Y.C., Lee, J.Y., Tsai, J.C., Prasad, I., Jinnai, H., Thomas, E.L., et al. (2020). Networks with controlled chirality via self-assembly of chiral triblock terpolymers. *Sci. Adv.* 6, eabc3644.
 40. Vaupotič, N., Salamończyk, M., Matraszek, J., Vogrin, M., Pociecha, D., and Gorecka, E. (2020). New structural model of a chiral cubic liquid crystalline phase. *Phys. Chem. Chem. Phys.* 22, 12814–12820.
 41. Newham, R.E. (2005). *Properties of Materials* (Oxford University Press).
 42. Palmer, D.C., and Salje, E.H. (1990). Phase transitions in leucite: dielectric properties and transition mechanism. *Phys. Chem. Minerals* 17, 444–452.
 43. Maldovan, M., Urbas, A.M., Yu, N., Carter, W.C., and Thomas, E.L. (2002). Photonic properties of bicontinuous cubic microphases. *Phys. Rev. B* 65, 165123.
 44. Lu, L., Fu, L., Joannopoulos, J.D., and Soljačić, M. (2013). Weyl points and line nodes in gyroid photonic crystals. *Nat. Photonics* 7, 294–299.
 45. Lu, L., Wang, Z., Ye, D., Ran, L., Fu, L., Joannopoulos, J.D., and Soljačić, M. (2015). Experimental observation of Weyl points. *Science* 349, 622–624.
 46. Turner, M.D., Saba, M., Zhang, Q., Cumming, B.P., Schröder-Turk, G.E., and Gu, M. (2013). Miniature chiral beamsplitter based on gyroid photonic crystals. *Nat. Photonics* 7, 801–805.
 47. Wang, S., Lee, S., Du, J.S., Partridge, B.E., Cheng, H.F., Zhou, W., Dravid, V.P., Lee, B., Glotzer, S.C., and Mirkin, C.A. (2022). The emergence of valency in colloidal crystals through electron equivalents. *Nat. Mater.* 21, 580–587.
 48. Feng, X., Burke, C.J., Zhuo, M., Guo, H., Yang, K., Reddy, A., Prasad, I., Ho, R.M., Avgeropoulos, A., Grason, G.M., et al. (2019). Seeing mesoatomic distortions in soft-matter crystals of a double-gyroid block copolymer. *Nature* 575, 175–179.
 49. Fogden, A., and Hyde, S.T. (1999). Continuous transformations of cubic minimal surfaces. *Eur. Phys. J. B* 7, 91–104.
 50. Schröder-Turk, G.E., Fogden, A., and Hyde, S.T. (2006). Bicontinuous geometries and molecular self-assembly: comparison of local curvature and global packing variations in genus-three cubic, tetragonal and rhombohedral surfaces. *Eur. Phys. J. B* 54, 509–524.
 51. Chen, H. (2021). Existence of the tetragonal and rhombohedral deformation families of the gyroid. *Indiana Univ. Math. J.* 70, 1543–1576.
 52. Hsueh, H.Y., Ling, Y.C., Wang, H.F., Chien, L.Y., Hung, Y.C., Thomas, E.L., and Ho, R.M. (2014).

- Shifting networks to achieve subgroup symmetry properties. *Adv. Mater.* 26, 3225–3229.
53. Mai, Y., and Eisenberg, A. (2012). Self-assembly of block copolymers. *Chem. Soc. Rev.* 41, 5969–5985.
54. Cao, Y., Yang, S., Li, Y., and Shi, J. (2021). Cooperative organizations of small molecular surfactants and amphiphilic block copolymers: roles of surfactants in the formation of binary co-assemblies. *Aggregate* 2.
55. Yang, S., Cao, Y., Wang, S., Li, Y., and Shi, J. (2022). Understanding on the surfactants engineered morphology evolution of block copolymer particles and their precise mesoporous silica replicas. *Chem. Res. Chin. Univ.* 38, 99–106.
56. Sakamoto, Y., Kaneda, M., Terasaki, O., Zhao, D.Y., Kim, J.M., Stucky, G., Shin, H.J., and Ryoo, R. (2000). Direct imaging of the pores and cages of three-dimensional mesoporous materials. *Nature* 408, 449–453.
57. Liu, Z., Fujita, N., Miyasaka, K., Han, L., Stevens, S.M., Suga, M., Asahina, S., Slater, B., Xiao, C., Sakamoto, Y., et al. (2013). A review of fine structures of nanoporous materials as evidenced by microscopic methods. *Microscopy* 62, 109–146.
58. Hovmöller, S. (1992). CRISP: crystallographic image processing on a personal computer. *Ultramicroscopy* 41, 121–135.
59. Han, L., Miyasaka, K., Terasaki, O., and Che, S. (2011). Evolution of packing parameters in the structural changes of silica mesoporous crystals: cage-type, 2D cylindrical, bicontinuous diamond and gyroid, and lamellar. *J. Am. Chem. Soc.* 133, 11524–11533.
60. Carlsson, A., Kaneda, M., Sakamoto, Y., Terasaki, O., Ryoo, R., and Joo, S.H. (1999). The structure of MCM-48 determined by electron crystallography. *J. Electron Microsc.* 48, 795–798.
61. Schumacher, K., Ravikovich, P.I., Du Chesne, A.D., Neimark, A.V., and Unger, K.K. (2000). Characterization of MCM-48 materials. *Langmuir* 16, 4648–4654.
62. Stefk, M., Mahajan, S., Sai, H., Epps, T.H., Bates, F.S., Gruner, S.M., DiSalvo, F.J., and Wiesner, U. (2009). Ordered three- and five-ply nanocomposites from ABC block terpolymer microphase separation with niobia and aluminosilicate sols. *Chem. Mater.* 21, 5466–5473.
63. Israelachvili, J.N., Mitchell, D.J., and Ninham, B.W. (1976). Theory of self-assembly of hydrocarbon amphiphiles into micelles and bilayers. *J. Chem. Soc. Faraday Trans. 2* 72, 1525–1568.
64. Lim, P.F.C., Chee, L.Y., Chen, S.B., and Chen, B.-H. (2003). Study of interaction between cetyltrimethylammonium bromide and poly(acrylic acid) by rheological measurements. *J. Phys. Chem. B* 107, 6491–6496.
65. Fundin, J., Hansson, P., Brown, W., and Lidegran, I. (1997). Poly(acrylic acid)–cetyltrimethylammonium bromide interactions studied using dynamic and static light scattering and time-resolved fluorescence quenching. *Macromolecules* 30, 1118–1126.
66. Cai, Y. (2022). Tilt modulus of bilayer membranes self-assembled from rod-coil diblock copolymers. *Langmuir* 38, 5820–5828.
67. Reddy, A., Dimitriev, M.S., and Grason, G.M. (2022). Medial packing and elastic asymmetry stabilize the double-gyroid in block copolymers. *Nat. Commun.* 13, 2629.
68. Seddon, A.M., Hallett, J., Beddoes, C., Plivelic, T.S., and Squires, A.M. (2014). Experimental confirmation of transformation pathways between inverse double diamond and gyroid cubic phases. *Langmuir* 30, 5705–5710.
69. Oka, T. (2015). Transformation between inverse bicontinuous cubic phases of a lipid from diamond to gyroid. *Langmuir* 31, 11353–11359.
70. Johnson, S., and Joannopoulos, J. (2001). Block-iterative frequency-domain methods for Maxwell's equations in a planewave basis. *Opt. Express* 8, 173–190.